

## Fully controlled photonic spin in highly confined optical field

Zhang, Shuoshuo; Fu, Shenggui; Zhang, Huanian; Ge, Xiaolu; Bai, Zhidong; Lyu, Yudong; Zhao, Rui; Man, Zhongsheng

**DOI**

[10.1364/OE.27.033621](https://doi.org/10.1364/OE.27.033621)

**Publication date**

2019

**Document Version**

Final published version

**Published in**

Optics Express

**Citation (APA)**

Zhang, S., Fu, S., Zhang, H., Ge, X., Bai, Z., Lyu, Y., Zhao, R., & Man, Z. (2019). Fully controlled photonic spin in highly confined optical field. *Optics Express*, 27(23), 33621-33633. <https://doi.org/10.1364/OE.27.033621>

**Important note**

To cite this publication, please use the final published version (if applicable). Please check the document version above.

**Copyright**

Other than for strictly personal use, it is not permitted to download, forward or distribute the text or part of it, without the consent of the author(s) and/or copyright holder(s), unless the work is under an open content license such as Creative Commons.

**Takedown policy**

Please contact us and provide details if you believe this document breaches copyrights. We will remove access to the work immediately and investigate your claim.



# Fully controlled photonic spin in highly confined optical field

SHUOSHUO ZHANG,<sup>1</sup> SHENGGUI FU,<sup>1,4</sup>  HUANIAN ZHANG,<sup>1</sup>  
XIAOLU GE,<sup>1</sup> ZHIDONG BAI,<sup>1</sup> YUDONG LYU,<sup>1</sup> RUI ZHAO,<sup>1</sup> AND  
ZHONGSHENG MAN<sup>1,2,3,5</sup> 

<sup>1</sup>*School of Physics and Optoelectronic Engineering, Shandong University of Technology, Zibo 255000, China*

<sup>2</sup>*Optics Research Group, Delft University of Technology, Department of Imaging Physics, Lorentzweg 1, 2628CJ Delft, The Netherlands*

<sup>3</sup>*Collaborative Innovation Center of Light Manipulations and Applications, Shandong Normal University, Jinan 250358, China*

<sup>4</sup>*fushenggui@sdut.edu.cn*

<sup>5</sup>*zsm@sdut.edu.cn*

**Abstract:** As an intrinsic attribute of light, the spin angular momentum (SAM) of photons has aroused considerable attention because of the fascinating properties emerging from light–matter interactions. We show that a diffraction-limited focal field with a steerable photonic spin structure in three dimensions can be produced under a  $4\pi$  microscopic system. This is achieved by focusing two counter-propagating configurable vector beams produced in the coherent superposition of three different beams with  $x$ -polarization,  $y$ -polarization, and radial-polarization. By altering the amplitude factors of these resultant beams, the ratios between the three mutually orthogonal polarized components can be freely tuned within the focal plane, thereby allowing dynamic control over the spin orientation and ellipticity of the tightly focused optical field. The results demonstrated in this paper may find applications in spin-controlled nanophotonics.

© 2019 Optical Society of America under the terms of the [OSA Open Access Publishing Agreement](#)

## 1. Introduction

Since the seminal work of Poynting [1] and the first experimental demonstration by Beth [2], it is well acknowledged that light carries both linear and angular momenta (AM). Generally, the AM of light can be separated into two distinct categories: spin angular momentum (SAM) and orbital angular momentum (OAM) [3]. These two components are the separately observable quantities in paraxial beams associated with the helicity (ellipticity) of the local polarization and the phase gradient induced by optical vortices, respectively [1–5]. When a light beam is circularly polarized, each of its photons carries a SAM of  $\pm\hbar$ , the sign is determined by the handedness of the polarization; here  $\hbar$  denotes the reduced Planck's constant [1,2]. The sign ambiguity reflects the SAM also being a vector; its direction is quantitatively described by the spin density [4,5]. From quantum mechanics and paraxial optics, we know that the SAM is purely longitudinal with its direction being aligned with the propagation axis because the electromagnetic field vectors are essentially confined to the transverse plane and thus describe two-dimensional fields.

However, in the optical fields with complex spatial distributions (i.e., three-dimensional (3D) vector fields), even if the propagation axis has been defined, the SAM takes any direction in three dimensions. That means light may potentially carry a transverse SAM in addition to its longitudinal counterpart. The appearance of a transverse SAM is strongly linked to the existence of longitudinal field components [4–16]. In particular, when the longitudinal and transverse field components are  $\pm\pi/2$  out of phase, the light is elliptically or circularly polarized in the meridional plane depending on the relative amplitudes of these two components, giving rise to a purely transverse SAM [4,5]. This extraordinary transverse spin can be typically formed in

various structured optical fields, including evanescent waves [6], surface plasmon polaritons [7,8], two-wave interference [9], and tightly focused beams [10–16]. In sharp contrast to what is known about photon spin, the transverse SAM, which exhibits a spin axis perpendicular to the direction of propagation, is either dependent or independent of the polarization helicity [6]. With such fascinating properties, light possessing transverse SAM has already found important applications in nano-optics, especially in the realm of spin-controlled directional emission and coupling [17–20]. Beyond that, the appearance of transverse SAM makes it possible to rotate small particles along a non-axial direction, which would provide additional rotational degrees of freedom for optical manipulations [12,21–23].

Although the transverse SAM enables various applications, a light field with a fully controlled spin structure may be more versatile in many scenarios. Over the past few years, fruitful endeavors allow the control of the spin orientation under nonparaxial conditions. As an intrinsic attribute, any prescribed spin state can be obtained theoretically by tailoring the states of polarization (SoPs) of light. For a nonparaxial beam with 3D controllable elliptical polarization, the spin orientation directly represented by the normal to the polarization plane is also unrestricted in 3D space. Such polarization states, as recently demonstrated in tight focusing systems, can be synthesized by reversing the radiation patterns from two electric dipoles [23–26] or by the assistance of a liquid crystal variable retarder [27]. These two methods provide an effective path for constructing arbitrary 3D polarization and spin in the focal region, but there are still a few drawbacks that deserve further study. First, the incident optical fields demonstrated in most of the preceding work are complicated in amplitude, phase, and polarization distributions because the focused fields are intimately linked to the initial forms. Second, the uniformity of the polarization distribution in the focal volume is almost unsatisfactory yielding a disorganized spin orientation and therefore constrains its use in many practical applications. Yan *et al.* proposed a structured incident light field to generate a focal spot with controllable 3D spin orientation and 3D super-resolution in a  $4\pi$  microscopic system [28]. This method greatly improves the uniformity of the spin orientation. However, ellipticity, as another important parameter of polarization, need also to be controlled to achieve a full manipulation of photonic spin.

In this context, by focusing two counter-propagating configurable vector beams in the  $4\pi$  microscopic system, we develop a novel method to control the spin orientation and ellipticity of a highly confined focused electric field. Here, the incident fields are constructed by the superposition of three distinct beams that possess separately  $x$ -polarization,  $y$ -polarization, and radial-polarization. According to the Richards–Wolf vectorial diffraction theory, the expressions of the electric field vectors near the focus are derived and presented in Section 2. Utilizing this established analytical modal, in Section 3, we investigate the focal behaviors of these resultant incident beams systematically. From the calculations, we see that a dynamic control over the spin orientation and ellipticity of the tightly focused electric field in the  $x$ - $y$  plane can be achieved by configuring the three amplitude factors of the incident beams. Finally, we summarize this work in Section 4.

## 2. Theoretical model

The key to achieving arbitrary 3D polarization states and spin orientations is to create three mutually orthogonal field components for which the amplitude and phase can be independently adjusted. Nevertheless, the electromagnetic wave nature in free space confines the polarization control to a plane. A way to break this limitation is to bend the wave front of light using a high numerical-aperture (NA) objective lens, which produces field components that are not contained in the input beams. This property is usually attributed to the depolarization effect of the focusing system [29,30]. For instance, a tightly focused radially polarized beam develops a robust longitudinal field component at the focal center, which enables a smaller focal spot and 3D control of polarization state [31–34]. Furthermore, because of the destructive interference

of radial components in the  $4\pi$  microscopic system, a purely longitudinal electric field with completely circular symmetry is formed in the focal plane by focusing two counter-propagating radially polarized beams with opposite instantaneous polarizations [35–38]. In contrast, when the objective is illuminated by a linearly polarized plane beam, the focused electric field is essentially dominated by the incident polarization, even though a relatively weak longitudinal field component is also produced out of focus [31,39].

Motivated by previous work, we constructed an incident optical field from the superposition of three different beams in a  $4\pi$  microscopic system. As sketched in Fig. 1, the three beams possess  $x$ -polarization,  $y$ -polarization, and radial-polarization, which are easily generated aided by two polarizers (P1, P2) and a radial-polarization converter (RPC). Subsequently, these beams are divided into two groups by three beam splitters (BS1, BS2, BS3) and directed by mirrors toward two oppositely placed high-NA objective lenses (Obj1, Obj2). Note that there is a phase difference of  $\pi$  between the two radially polarized beams whereas the left and right parts of the linearly polarized beams are in phase. Each group of beams is finally focused by the high-NA objectives and made to interfere isotropically in the confocal region to create three mutually orthogonal electric-field components with independently controllable amplitudes and phases. According to the Richards–Wolf vectorial diffraction theory [40], for the three kinds of the incident beams on the left side, the electric-field vectors at observation point  $Q$  ( $\rho_Q, \phi_Q, z_Q$ ) in the focal volume may be expressed as

$$\begin{bmatrix} \mathbf{E}_{L1}(\rho_Q, \phi_Q, z_Q) \\ \mathbf{E}_{L2}(\rho_Q, \phi_Q, z_Q) \\ \mathbf{E}_{L3}(\rho_Q, \phi_Q, z_Q) \end{bmatrix} = iA \int_0^{2\pi} \int_0^{\theta_{\max}} l(\theta) \cos^{1/2} \theta \mathbf{M} \begin{bmatrix} \mathbf{p}_1 \\ \mathbf{p}_2 \\ \mathbf{p}_3 \end{bmatrix} e^{ik[-\rho_Q \sin \theta \cos(\varphi - \phi_Q) + z_Q \cos \theta]} \sin \theta d\theta d\varphi, \quad (1)$$

and for the incident beams on the right side, the electric-field vectors at the observation point may be expressed as

$$\begin{bmatrix} \mathbf{E}_{R1}(\rho_Q, \phi_Q, z_Q) \\ \mathbf{E}_{R2}(\rho_Q, \phi_Q, z_Q) \\ \mathbf{E}_{R3}(\rho_Q, \phi_Q, z_Q) \end{bmatrix} = iA \int_0^{2\pi} \int_0^{\theta_{\max}} l(\theta) \cos^{1/2} \theta \mathbf{M} \begin{bmatrix} \mathbf{q}_1 \\ \mathbf{q}_2 \\ \mathbf{q}_3 \end{bmatrix} e^{ik[-\rho_Q \sin \theta \cos(\varphi - \phi_Q) - z_Q \cos \theta]} \sin \theta d\theta d\varphi, \quad (2)$$

where subscripts 1, 2, and 3 refer to the corresponding focal fields of the  $x$ -polarized,  $y$ -polarized, and radially-polarized components of the incident beams, respectively;  $A$  is a constant that is set to 1 in our configuration, and  $\theta_{\max} = \sin^{-1}(\text{NA}/n)$  is the maximum convergence angle with NA the numerical aperture of the focusing lens and  $n$  the refractive index in the image space. The relative amplitude distribution,  $l(\theta)$ , of the incident optical field is taken to be [31]

$$l(\theta) = \exp \left[ -\beta_0^2 \left( \frac{\sin \theta}{\text{NA}/n} \right)^2 \right] J_m \left( 2\beta_0 \frac{\sin \theta}{\text{NA}/n} \right), \quad (3)$$

where  $\beta_0$  is defined as the ratio between the pupil radius and the beam waist, and  $J_m(\cdot)$  is the  $m$ th-order Bessel function of the first kind. By increasing the value of  $m$ , the radius of the dark region at the center of the incident beam is also increased, so that only the rays with a large convergence angle are focused by the objectives, which causes a higher effective NA. In other words, a diffraction-limited focused electric field in three dimensions can be produced in the confocal region of the  $4\pi$  microscopic system by properly optimizing the value of  $m$ . Throughout this paper,  $\beta_0 = 1$ ,  $\text{NA} = 0.95$ ,  $m = 2$ , and  $n = 1$  are selected.

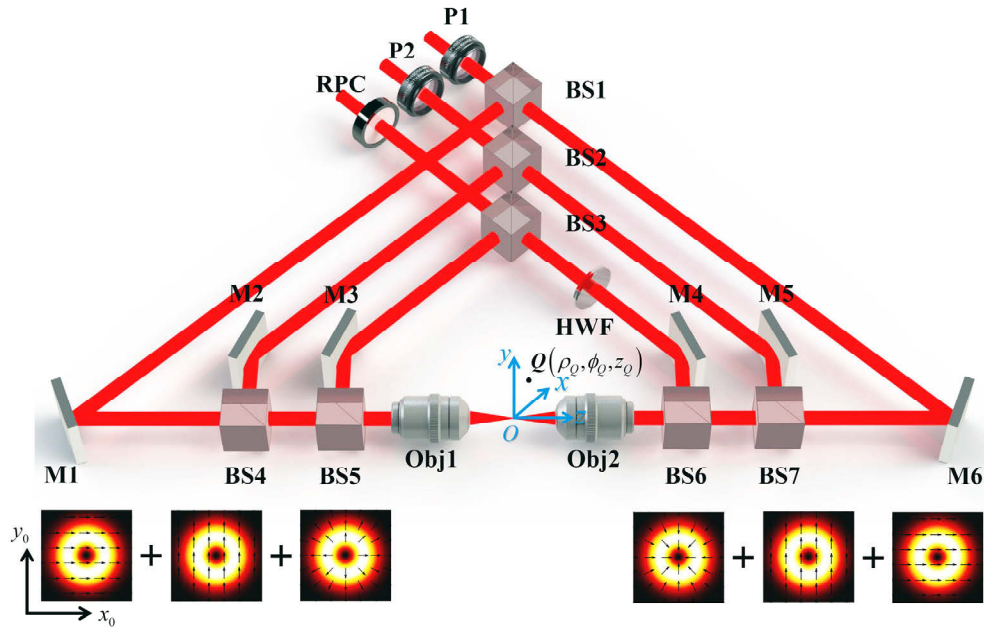


**Fig. 1.** Schematic illustration of the optical scheme for achieving a diffraction-limited focal field with arbitrary controlled photonic spin. P, polarizer; RPC, radial polarization converter; BS, beam splitter; HWP, half-wave plate; M, mirror; Obj, objective.

In Eqs. (1) and (2), the matrix  $\mathbf{M}$  is defined as

$$\mathbf{M} = \begin{bmatrix} \xi \exp(i\delta_x) & 0 & 0 \\ 0 & \eta \exp(i\delta_y) & 0 \\ 0 & 0 & \zeta \end{bmatrix}, \quad (4)$$

where  $\xi$ ,  $\eta$ , and  $\zeta$  are the amplitude factors, which may be varied from 0 to 1;  $\delta_x$  and  $\delta_y$  are the initial phases of the corresponding incident beams;  $\mathbf{p}_1$ ,  $\mathbf{p}_2$ , and  $\mathbf{p}_3$  represent the polarization unit vectors in the image space determined by the input polarization states of the incident beams on the left-hand side, their three mutually orthogonal Cartesian components are found to be

$$\begin{bmatrix} p_{1x} \\ p_{1y} \\ p_{1z} \end{bmatrix} = \begin{bmatrix} \sin^2 \varphi + \cos \theta \cos^2 \varphi \\ (\cos \theta - 1) \sin \varphi \cos \varphi \\ \sin \theta \cos \varphi \end{bmatrix}, \quad (5)$$

$$\begin{bmatrix} p_{2x} \\ p_{2y} \\ p_{2z} \end{bmatrix} = \begin{bmatrix} (\cos \theta - 1) \sin \varphi \cos \varphi \\ \sin^2 \varphi + \cos \theta \cos^2 \varphi \\ \sin \theta \sin \varphi \end{bmatrix}, \quad (6)$$

$$\begin{bmatrix} p_{3x} \\ p_{3y} \\ p_{3z} \end{bmatrix} = \begin{bmatrix} \cos \theta \cos \varphi \\ \cos \theta \sin \varphi \\ \sin \theta \end{bmatrix}, \quad (7)$$

and the Cartesian components of the polarization unit vector  $\mathbf{q}_1$ ,  $\mathbf{q}_2$ , and  $\mathbf{q}_3$  associated with the incident beams on the right-hand side can be obtained through the following transformation rules:

$$\begin{bmatrix} q_{1x} \\ q_{1y} \\ q_{1z} \end{bmatrix} = \begin{bmatrix} 1 & 0 & 0 \\ 0 & 1 & 0 \\ 0 & 0 & -1 \end{bmatrix} \begin{bmatrix} p_{1x} \\ p_{1y} \\ p_{1z} \end{bmatrix}, \quad (8)$$

$$\begin{bmatrix} q_{2x} \\ q_{2y} \\ q_{2z} \end{bmatrix} = \begin{bmatrix} 1 & 0 & 0 \\ 0 & 1 & 0 \\ 0 & 0 & -1 \end{bmatrix} \begin{bmatrix} p_{2x} \\ p_{2y} \\ p_{2z} \end{bmatrix}, \quad (9)$$

$$\begin{bmatrix} q_{3x} \\ q_{3y} \\ q_{3z} \end{bmatrix} = \begin{bmatrix} -1 & 0 & 0 \\ 0 & -1 & 0 \\ 0 & 0 & 1 \end{bmatrix} \begin{bmatrix} p_{3x} \\ p_{3y} \\ p_{3z} \end{bmatrix}. \quad (10)$$

The total electric field at the observation point is, of course, the vector sum of the focal fields contributed by the left and right incident beams, namely,

$$\mathbf{E}(\rho_Q, \phi_Q, z_Q) = \mathbf{E}_L(\rho_Q, \phi_Q, z_Q) + \mathbf{E}_R(\rho_Q, \phi_Q, z_Q). \quad (11)$$

For a field described in three dimensions, the polarization description is no longer confined to the transverse plane. Like the highly confined focused field of this study, the electric field  $\mathbf{E}$  at each point is, in general, oscillating in a plane of arbitrary direction in 3D space. Under this circumstance, the local state of the polarization can be characterized by a 3D polarization ellipse for which the major axis  $\Lambda_1$  and minor axis  $\Lambda_2$  are defined in [41–43]

$$\Lambda_1 = \frac{1}{\sqrt{\mathbf{E} \cdot \mathbf{E}}} \operatorname{Re} \left( \mathbf{E}^* \sqrt{\mathbf{E} \cdot \mathbf{E}} \right), \quad (12)$$

and

$$\Lambda_2 = \frac{1}{\sqrt{\mathbf{E} \cdot \mathbf{E}}} \operatorname{Im} \left( \mathbf{E}^* \sqrt{\mathbf{E} \cdot \mathbf{E}} \right), \quad (13)$$

respectively, with the superscripted asterisk ‘\*’ denoting the operation of complex conjugation. In Eqs. (12) and (13),  $\Lambda_1$  and  $\Lambda_2$  are recognized as vectors carrying both magnitude and direction. However, by convention, these two quantities are generally described as scalar lines because the polarization ellipse is indistinguishable under a  $\pi$  rotation in its plane. This divergence is also reflected by the sign ambiguity associated with the square roots in the equations. Furthermore, the ellipticity of the polarization ellipse at each point may be calculated from

$$\varepsilon = \pm \tan^{-1}(\Lambda_2/\Lambda_1), \quad (14)$$

where  $\Lambda_1$  and  $\Lambda_2$  are the moduli of the corresponding complex vectors. As there are two opposing conventions for determining the handedness of the elliptical or circular polarization, we specify that the sign in Eq. (14) should be positive for right-handedness and negative for left-handedness, with the handedness defined relative to that of the light source.

### 3. Results and discussion

Based on Eqs. (1)–(14), we first analyze the intensity and polarization characteristics of the focused electric field in the proposed  $4\pi$  microscopic system. As an example, Fig. 2(a) gives the normalized electric field distribution in the confocal region when the two counter-propagating incident beams are configured with  $(\xi, \eta, \zeta) = (1, 1, 1)$ . To generate the desired 3D elliptical polarization, the initial phases of the two linearly-polarized components of the incident beams are assumed to be  $-\pi/4$  and  $\pi/4$ , respectively. As depicted in Fig. 2(a), both intensity and polarization distributions are projected onto three orthogonal planes. The latter is indicated by the polarization ellipses, where blue and red representing left- and right-handedness, respectively. The main lobe of the focal spot, which is defined by the full-width at half-maximum (FWHM) of the intensity, is enclosed by the white contour. Clearly, the polarization distribution within the main lobe exhibits good uniformity, which is not only limited to the focal plane ( $x$ - $y$  plane) but also to the through-focus planes ( $x$ - $z$  and  $y$ - $z$  planes). As uniformity is crucial for many practical applications, in some sense, it also enhances the feasibility and superiority of our strategy.

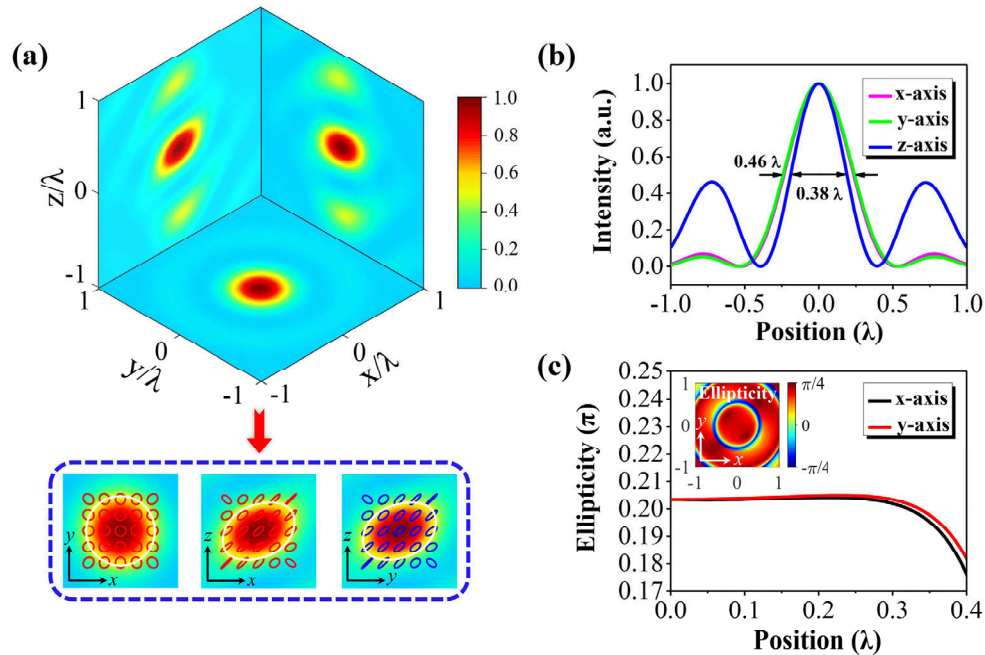


**Fig. 2.** Focal behaviors of the two counter-propagating configurable vector beams with  $(\xi, \eta, \zeta; \delta_x, \delta_y) = (1, 1, 1; -\pi/4, \pi/4)$ . (a) Normalized intensity distributions of the focal electric field, as well as the polarization projections in three orthogonal planes. The white contour encloses the area defined by the full-width at half-maximum (FWHM). (b) Line scans of the intensity distributions along the  $x$ -,  $y$ -, and  $z$ -axes. (c) Ellipticity of the 3D polarization ellipses in the  $x$ - $y$  plane.

To evaluate the resolution of the focal spot, the line scans of the intensity along the  $x$ -,  $y$ -, and  $z$ -axis are demonstrated in Fig. 2(b), from which the FWHMs are calculated to be  $0.46\lambda$ ,  $0.46\lambda$ , and  $0.38\lambda$ , respectively. Although there are significant side lobes along the  $z$ -axis, the focal spot is 3D super-resolved because all three dimensions are smaller than the Abbe diffraction limit determined by  $\lambda/2NA \approx 0.526\lambda$ . Recall that diffraction-limited focal fields have potential applications in ultra-density optical data storage and super-resolution microscopic imaging. In our case, the side lobes are mainly caused by the destructive interference of the focused beams

and may be minimized by further increasing the order of the Bessel function [see Eq. (3)] but at the expense of the reduced axial resolution. With the sample generally placed on the focal plane during light–matter interactions, in the following sections, we confine our discussion to the focused electric field in the  $x$ - $y$  plane. The ellipticity of the 3D polarization ellipses in the  $x$ - $y$  plane was calculated from Eqs. (12)–(14) and illustrated in Fig. 2(c). From the curves, one finds that the ellipticity is nearly constant over a radius of  $0.3\lambda$  due to the similar distributions of the three Cartesian components of the electric field.

A detailed analysis of the polarization projections in the  $x$ - $y$  plane may be performed invoking the three normalized Stokes parameters [44],  $S_1$ ,  $S_2$ , and  $S_3$ , which are widely used to describe the spatial distribution of SoPs in a 2D vector field. As the electric field is a function of coordinates  $(x, y)$ , the calculated Stokes parameters also vary spatially. As evident from Figs. 3(a1)–3(a3), the values of  $S_3$  in the main lobe are near maximum whereas those of  $S_1$  and  $S_2$  are nearly zero, indicating that most of the polarization projections in the  $x$ - $y$  plane are in a right-handed circular polarization state, which is in good agreement with what is displayed in Fig. 1(a). Unlike the aforementioned Stokes parameters, the spin (AM) density can be used to characterize the SoPs in three dimensions. Although both electric and magnetic fields contribute to the spin density, only the electric part is considered in this study because the most common materials are nonmagnetic and react primarily to the local electric field in the light–matter interactions. Thus, the spin density may be expressed as [23,26]

$$\mathbf{S} \propto \text{Im}(\mathbf{E}^* \times \mathbf{E}). \quad (15)$$

The spin density is obviously a vector along the normal direction of the polarization ellipse with its magnitude being proportional to the local ellipticity. In other words, the magnitude of the spin density is zero for the point corresponding to linear polarization and attains its maximum at the point corresponding to circular polarization. When considering a small particle placed in a light field that exhibits nonzero spin density, the particle rotates along one of its own axes as SAM is transferred to the trapped one. From the literature, we know that such a spin axis is consistent with the direction of the SAM and may be derived from the spin density. To describe the orientation of the spin axis quantitatively, we define the direction angles with respect to the three axes as

$$\begin{cases} \alpha = \cos^{-1} \left( S_x / \sqrt{S_x^2 + S_y^2 + S_z^2} \right) \\ \beta = \cos^{-1} \left( S_y / \sqrt{S_x^2 + S_y^2 + S_z^2} \right) \\ \gamma = \cos^{-1} \left( S_z / \sqrt{S_x^2 + S_y^2 + S_z^2} \right) \end{cases}. \quad (16)$$

The normalized spin density of the focused beam [Fig. 2(a)], as well as the direction angles of the spin axis, are presented in Figs. 3(b1)–3(b3) and 3(c1)–3(c3), respectively. As implied in Eq. (15), we see that all the components of the spin density in the  $x$ - $y$  plane exist simultaneously and exhibit nearly symmetric profiles due to the nonzero and symmetric distributions of the three electric-field components and their phase differences. Here, the sign of the spin density reflects the handedness of the 2D field polarization (i.e., the polarization projections onto the three planes), which is positive for right-handedness and negative for left-handedness. In Figs. 3(b1)–3(b3), the  $z$ -component of the normalized spin density is positive and much stronger than the  $x$  and  $y$  components with negative values. Consequently, the orientation of the spin axis is somewhat closer to the  $+z$  axis in 3D space. This conclusion is supported by the three direction angles calculated from Eq. (16). Because the polarization distribution shows good uniformity in the main lobe, without loss of generality, we extract the value at the geometric focus to represent the spin orientation of the whole region. As revealed from Fig. 3(c1)–3(c3), the spin axis at the geometric focus is directed along  $(\alpha, \beta, \gamma) = (118^\circ, 118^\circ, 42^\circ)$ .

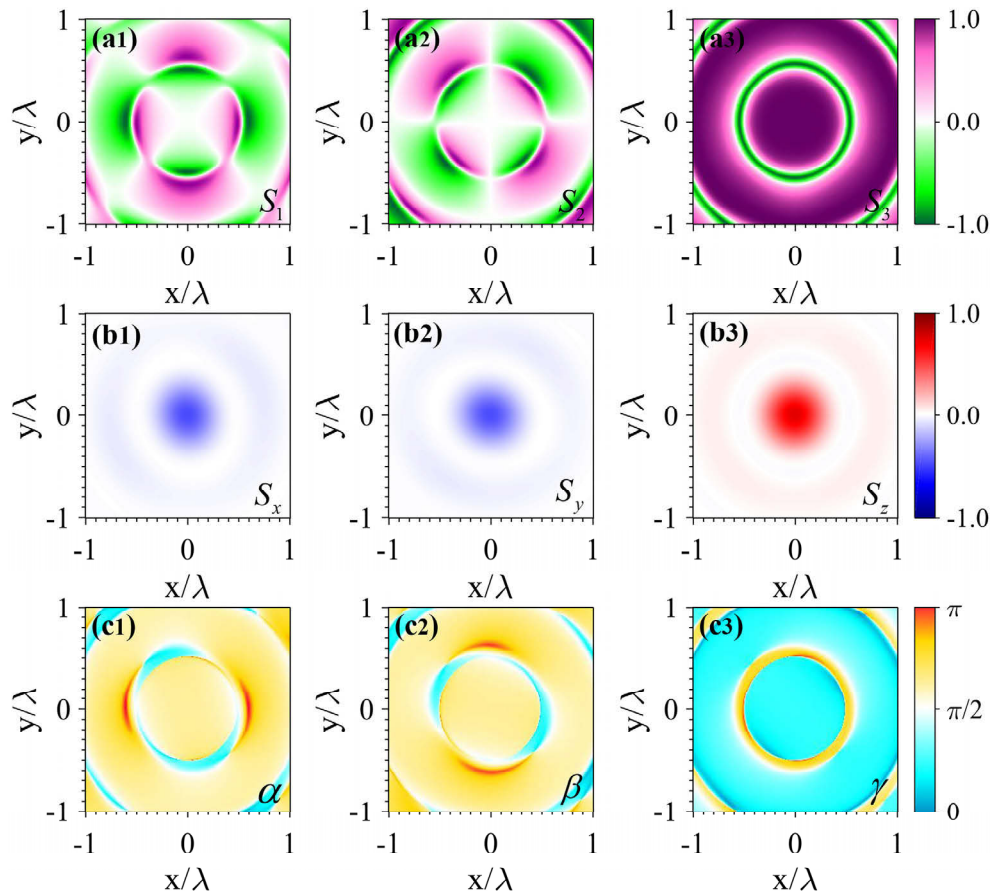


**Fig. 3.** Polarization and spin characteristics in the  $x$ - $y$  plane of the highly confined optical field depicted in Fig. 2(a): (a1)–(a3) normalized Stokes parameters; (b1)–(b3) spin density components; (c1)–(c3) direction angles used to quantify the orientation of the spin axis.

Given the theoretical analysis of Section 2, we know that by configuring the three amplitude factors ( $\xi$ ,  $\eta$ ,  $\zeta$ ) of the incident beams, the ratios between the three mutually orthogonal field components within the focal plane can be freely tuned to construct any desired 3D elliptical polarization, which yields a steerable spin orientation in three dimensions. To demonstrate the feasibility of our strategy, here we consider three limiting cases of the amplitude factors in the range  $[0, 1]$ , i.e.,  $(\xi, \eta, \zeta) = (0, 1, 1)$ ,  $(1, 0, 1)$ , and  $(1, 1, 0)$ , respectively. For all the calculations,  $(\delta_x, \delta_y) = (-\pi/4, \pi/4)$  remains fixed. The 3D polarization distributions in the  $x$ - $y$  plane corresponding to the three cases are given in Fig. 4(a)–4(c). As specified earlier, the left-handed and right-handed elliptical polarizations are marked in blue and red, respectively; their projections are shown in green. As one of the electric field components vanishes, the newly synthesized polarization ellipse is parallel to the  $y$ - $z$  plane [Fig. 4(a)], the  $x$ - $z$  plane [Fig. 4(b)], and the  $x$ - $y$  plane [Fig. 4(c)]. Therefore, the spin orientation represented by the normal direction of the polarization plane is collinear with the three coordinate axes, as indicated by black arrows. To analyze the spin characteristics of the focused field further, the normalized spin densities of the three cases are calculated and demonstrated in the last three rows in Fig. 4. As expected, for each case, there is only one obvious component present, whereas the other two components are negligible or vanish completely. Note that even if the  $x$ -polarized component of the incident

beams is blocked in the first case ( $\xi = 0$ ), the incident y-polarized beams can also produce an  $E_x$  component via the inherent depolarization effect. This is why  $S_y$  and  $S_z$  are non-zero in the  $x$ - $y$  plane. Of course, the  $E_x$  component produced is fairly weak ( $\sim 10\%$ ) compared with the  $E_y$  component and is distributed mainly in the region outside of the focus. Hence, the effect on the spin orientation within the main lobe is negligible. A similar explanation also applies to the second case.

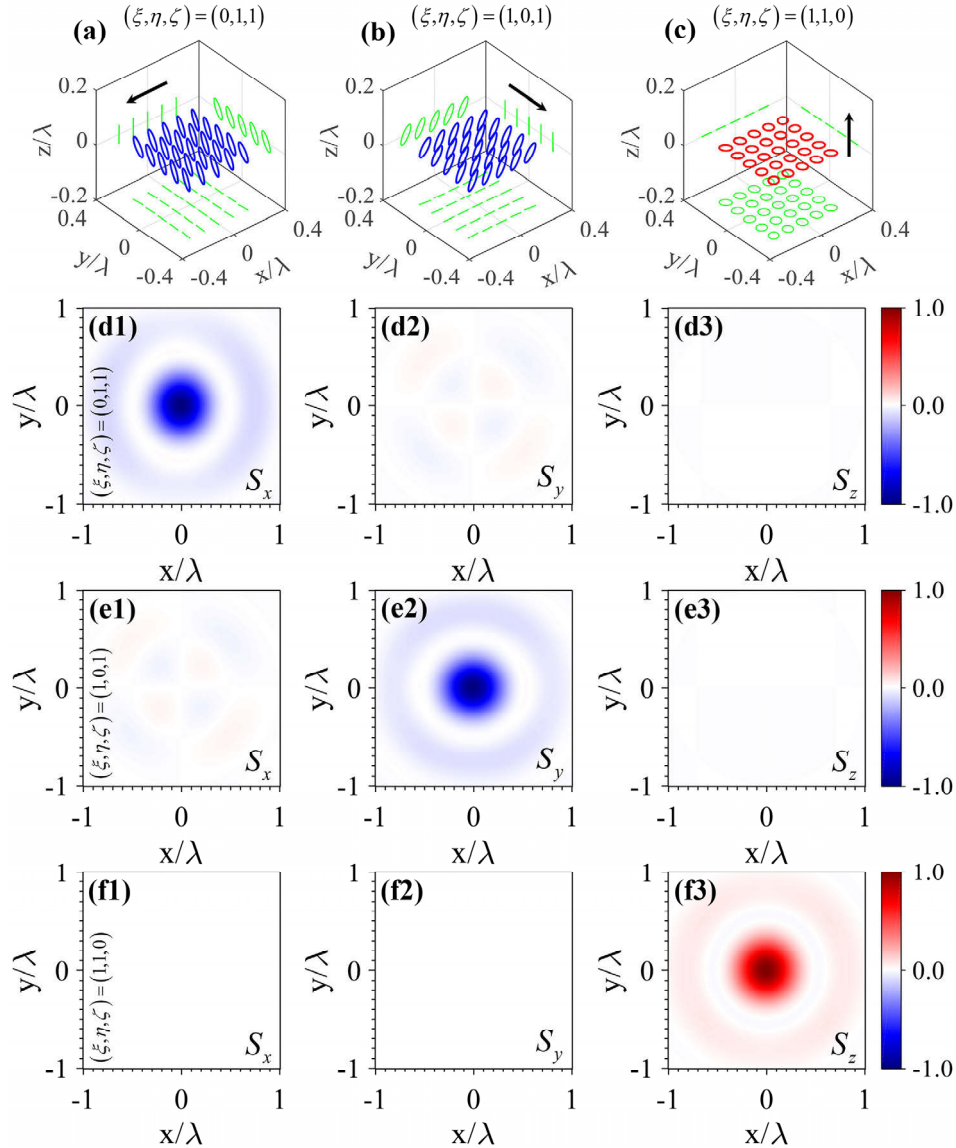


**Fig. 4.** 3D polarization distributions in the  $x$ - $y$  plane and their projections in the three orthogonal planes with  $(\xi, \eta, \zeta) =$  (a)  $(0, 1, 1)$ , (b)  $(1, 0, 1)$ , and (c)  $(1, 1, 0)$ . The black arrows indicate the orientation of the spin axis. (d1)–(d3) Spin density components with  $(\xi, \eta, \zeta) = (0, 1, 1)$ . (e1)–(e3) Spin density components with  $(\xi, \eta, \zeta) = (1, 0, 1)$ . (f1)–(f3) Spin density components with  $(\xi, \eta, \zeta) = (1, 1, 0)$ . For all calculations,  $(\delta_x, \delta_y) = (-\pi/4, \pi/4)$  is chosen.

Next, we discuss the correlation between the spin orientation in the  $x$ - $y$  plane and the three amplitude factors of the incident beams. By varying the amplitude factors from 0 to 1, the direction angles  $\alpha$ ,  $\beta$ , and  $\gamma$ , which are used to quantify the orientation of the spin axis, take values in the ranges of  $[90^\circ, 180^\circ]$ ,  $[90^\circ, 180^\circ]$ , and  $[0^\circ, 90^\circ]$ , respectively [see Figs. 5(a), 5(c), and 5(e)]. By reversing the handedness of the polarization ellipse, the control of the three direction angles can be further extended to  $[0^\circ, 180^\circ]$ . That is to say, the spin orientation of the focused field in this work is unlimited in 3D space. Indeed, an optical field with fully controlled spin structure is more versatile in many practical applications than fields with purely longitudinal or purely transverse SAM. In addition, the evolutions of ellipticity in the  $x$ - $y$  plane with respect to the three amplitude factors [Figs. 5(b), 5(d), and 5(f)] clearly show ellipticity decreasing (increasing) with increasing  $\zeta$  ( $\xi$  and  $\eta$ ). The tuning range is  $[0.124\pi, 0.249\pi]$ , which is not immutable and depends on the phase differences between the three electric-field components determined by the initial phases  $\delta_x$  and  $\delta_y$ .

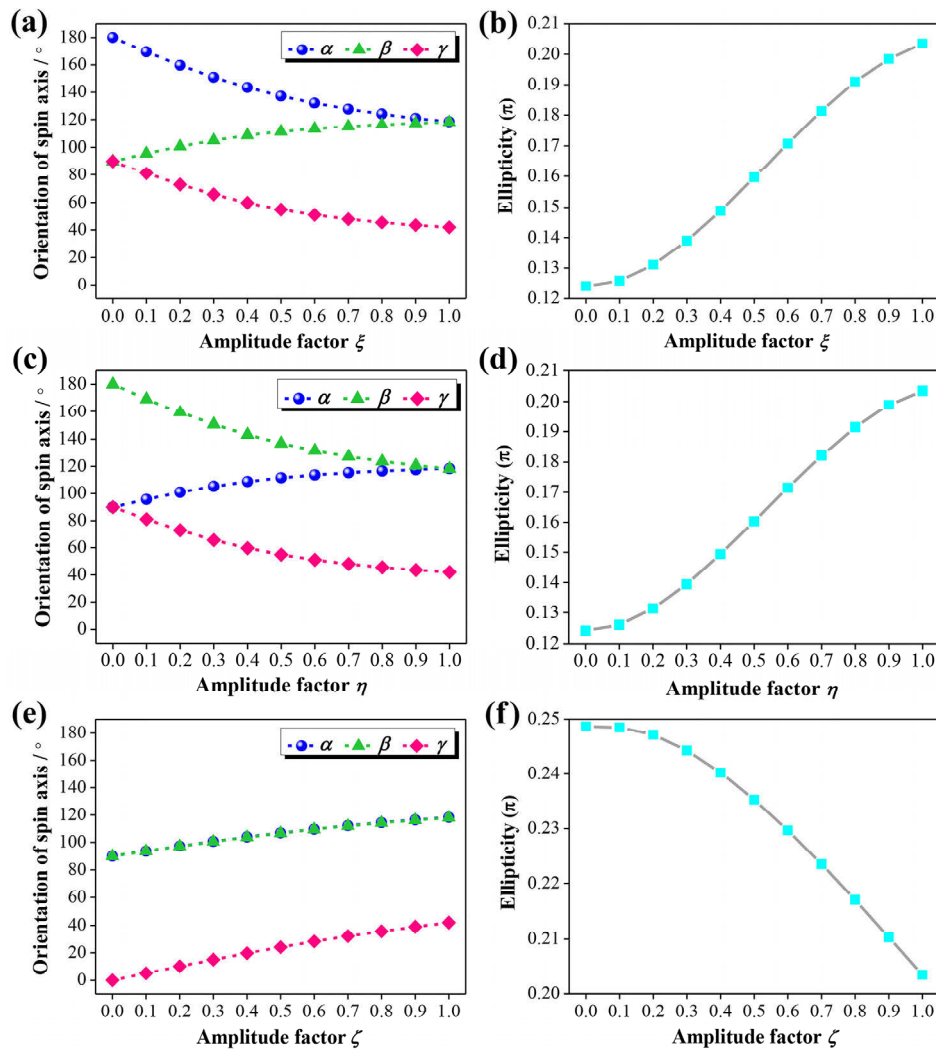


**Fig. 5.** Evolutions of the spin orientation and ellipticity in the  $x$ - $y$  plane versus the amplitude factors of the incident beams. In (a) and (b),  $\eta = \zeta = 1$ . In (c) and (d),  $\xi = \zeta = 1$ . In (e) and (f),  $\xi = \eta = 1$ . For all calculations,  $(\delta_x, \delta_y) = (-\pi/4, \pi/4)$  is chosen.

#### 4. Conclusion

We have theoretically demonstrated a novel and effective method to control the spin orientation and ellipticity within a highly confined focused field. The key to this method is to create three mutually orthogonal and independent electric-field components (i.e.,  $E_x$ ,  $E_y$ , and  $E_z$ ) in the focal region by focusing two counter-propagating incident beams in a  $4\pi$  microscopic system. Toward this end, the single incident field is constructed by the superposition of three distinct beams possessing  $x$ -polarization,  $y$ -polarization, and radial-polarization, separately. From the Richards–Wolf vectorial diffraction theory, expressions for the electric field vectors near the focus were derived to evaluate the focal behaviors of these newly resultant incident beams. Using calculations, we find that the focal spot obtained in this work is 3D super-resolved because all three dimensions are smaller than the diffraction limit ( $\sim 0.526\lambda$ ). The FWHMs along the  $x$ -,  $y$ -, and  $z$ -axes are  $0.46\lambda$ ,  $0.46\lambda$ , and  $0.38\lambda$ , respectively. More importantly, the polarization distribution within the main lobe exhibits excellent uniformity in both the focal plane ( $x$ - $y$  plane) and the through-focus planes ( $x$ - $z$  and  $y$ - $z$  planes), which yields an organized spin orientation of the focused beam. The spin characteristics of the focused beam were analyzed in detail using the well-defined spin density. The calculations reveal that there is a strong correlation between the spin orientation in the  $x$ - $y$  plane and the three amplitude factors ( $\xi$ ,  $\eta$ , and  $\zeta$ ) of the incident beams. As the amplitude factors vary from 0 to 1, the three direction angles  $\alpha$ ,  $\beta$ , and  $\gamma$ , which are used to quantify the orientation of the spin axis, continuously change over the intervals  $[90^\circ, 180^\circ]$ ,  $[90^\circ, 180^\circ]$ , and  $[0^\circ, 90^\circ]$ , respectively. By reversing the handedness of the polarization ellipse, the control of the three direction angles can be further extended to  $[0^\circ, 180^\circ]$ , meaning the spin orientation is unrestricted in 3D space. Moreover, the tuning range of the ellipticity in the  $x$ - $y$  plane is  $[0.124\pi, 0.249\pi]$ , which depends on the phase differences between the three electric-field components. The results demonstrated in this work opens up new avenues for manipulating the spin structure and ellipticity within a highly confined optical field, which may find important applications in optical tweezers as well as spin-controlled directional emission and coupling. It should also be emphasized that the incident multiple beams need to be precisely aligned in practical applications.

#### Funding

National Natural Science Foundation of China (11604182, 11704226); Natural Science Foundation of Shandong Province (ZR2016AB05); Natural Science Foundation of Shandong Province (ZR2017MA051).

#### Disclosures

The authors declare no conflicts of interest

#### References

1. J. H. Poynting, "The wave-motion of a revolving shaft, and a suggestion as to the angular momentum in a beam of circularly-polarized light," *Proc. R. Soc. London, Ser. A* **82**(557), 560–567 (1909).
2. R. A. Beth, "Mechanical detection and measurement of the angular momentum of light," *Phys. Rev.* **50**(2), 115–125 (1936).
3. L. Allen, M. W. Beijersbergen, R. J. C. Spreeuw, and J. P. Woerdman, "Orbital angular momentum of light and the transformation of Laguerre–Gaussian laser modes," *Phys. Rev. A* **45**(11), 8185–8189 (1992).
4. A. Aiello, P. Banzer, M. Neugebauer, and G. Leuchs, "From transverse angular momentum to photonic wheels," *Nat. Photonics* **9**(12), 789–795 (2015).
5. K. Y. Bliokh and F. Nori, "Transverse and longitudinal angular momenta of light," *Phys. Rep.* **592**, 1–38 (2015).
6. K. Y. Bliokh, A. Y. Bekshaev, and F. Nori, "Extraordinary momentum and spin in evanescent waves," *Nat. Commun.* **5**(1), 3300 (2014).
7. K. Y. Bliokh and F. Nori, "Transverse spin of a surface polariton," *Phys. Rev. A* **85**(6), 061801 (2012).
8. A. Canaguier-Durand and C. Genet, "Transverse spinning of a sphere in a plasmonic field," *Phys. Rev. A* **89**(3), 033841 (2014).

9. A. Y. Bekshaev, K. Y. Bliokh, and F. Nori, "Transverse Spin and Momentum in Two-Wave Interference," *Phys. Rev. X* **5**(1), 011039 (2015).
10. S. Winnerl, R. Hubrich, M. Mittendorff, H. Schneider, and M. Helm, "Universal phase relation between longitudinal and transverse fields observed in focused terahertz beams," *New J. Phys.* **14**(10), 103049 (2012).
11. M. Neugebauer, P. Banzer, T. Bauer, S. Orlov, N. Lindlein, A. Aiello, and G. Leuchs, "Geometric spin Hall effect of light in tightly focused polarization-tailored light beams," *Phys. Rev. A* **89**(1), 013840 (2014).
12. M. Neugebauer, T. Bauer, P. Banzer, and G. Leuchs, "Polarization tailored light driven directional optical nanobeacon," *Nano Lett.* **14**(5), 2546–2551 (2014).
13. W. Zhu, V. Shvedov, W. She, and W. Krolkowski, "Transverse spin angular momentum of tightly focused full Poincaré beams," *Opt. Express* **23**(26), 34029–34041 (2015).
14. M. Neugebauer, T. Bauer, A. Aiello, and P. Banzer, "Measuring the transverse spin density of light," *Phys. Rev. Lett.* **114**(6), 063901 (2015).
15. M. Neugebauer, J. S. Eismann, T. Bauer, and P. Banzer, "Magnetic and Electric Transverse Spin Density of Spatially Confined Light," *Phys. Rev. X* **8**(2), 021042 (2018).
16. P. Yu, Q. Zhao, X. Hu, Y. Li, and L. Gong, "Orbit-induced localized spin angular momentum in tight focusing of linearly polarized vortex beams," *Opt. Lett.* **43**(22), 5677–5680 (2018).
17. F. J. Rodríguez-Fortuño, G. Marino, P. Ginzburg, D. O'Connor, A. Martínez, G. A. Wurtz, and A. V. Zayats, "Near-field interference for the unidirectional excitation of electro-magnetic guided modes," *Science* **340**(6130), 328–330 (2013).
18. J. Petersen, J. Volz, and A. Rauschenbeutel, "Chiral nanophotonic waveguide interface based on spin-orbit interaction of light," *Science* **346**(6205), 67–71 (2014).
19. L. Marrucci, "Quantum optics: spin gives direction," *Nat. Phys.* **11**(1), 9–10 (2015).
20. Y. Lefier and T. Grosjean, "Unidirectional sub-diffraction waveguiding based on optical spin-orbit coupling in subwavelength plasmonic waveguides," *Opt. Lett.* **40**(12), 2890–2893 (2015).
21. K.-Y. Kim and S. Kim, "Spinning of a submicron sphere by Airy beams," *Opt. Lett.* **41**(1), 135–138 (2016).
22. M. Li, S. Yan, Y. Liang, P. Zhang, and B. Yao, "Transverse spinning of particles in highly focused vector vortex beams," *Phys. Rev. A* **95**(5), 053802 (2017).
23. G. Rui, Y. Li, S. Zhou, Y. Wang, B. Gu, Y. Cui, and Q. Zhan, "Optically induced rotation of Rayleigh particles by arbitrary photonic spin," *Photonics Res.* **7**(1), 69–79 (2019).
24. W. Chen and Q. Zhan, "Diffraction limited focusing with controllable arbitrary three-dimensional polarization," *J. Opt.* **12**(4), 045707 (2010).
25. W. Chen and Q. Zhan, "Three-dimensional polarization control in 4Pi microscopy," *Opt. Commun.* **284**(1), 52–56 (2011).
26. J. Chen, C. Wan, L. Kong, and Q. Zhan, "Tightly focused optical field with controllable photonic spin orientation," *Opt. Express* **25**(16), 19517–19528 (2017).
27. W. Zhu and W. She, "Generation of tunable three-dimensional polarization in 4Pi focusing system," *Opt. Express* **21**(14), 17265–17274 (2013).
28. W. Yan, Z. Nie, X. Liu, X. Zhang, Y. Wang, and Y. Song, "Arbitrary spin-orientated and super-resolved focal spot," *Opt. Lett.* **43**(16), 3826–3829 (2018).
29. J. W. M. Chon, X. Gan, and M. Gu, "Splitting of the focal spot of a high numerical-aperture objective in free space," *Appl. Phys. Lett.* **81**(9), 1576–1578 (2002).
30. D. Ganic, X. Gan, and M. Gu, "Focusing of doughnut laser beams by a high numerical-aperture objective in free space," *Opt. Express* **11**(21), 2747–2752 (2003).
31. K. Youngworth and T. Brown, "Focusing of high numerical aperture cylindrical-vector beams," *Opt. Express* **7**(2), 77–87 (2000).
32. Q. Zhan and J. R. Leger, "Focus shaping using cylindrical vector beams," *Opt. Express* **10**(7), 324–331 (2002).
33. R. Dorn, S. Quabis, and G. Leuchs, "Sharper focus for a radially polarized light beam," *Phys. Rev. Lett.* **91**(23), 233901 (2003).
34. Y. Kozawa and S. Sato, "Focusing property of a double-ring-shaped radially polarized beam," *Opt. Lett.* **31**(6), 820–822 (2006).
35. Z. Chen and D. Zhao, "4Pi focusing of spatially modulated radially polarized vortex beams," *Opt. Lett.* **37**(8), 1286–1288 (2012).
36. G. Chen, F. Song, and H. Wang, "Sharper focal spot generated by  $4\pi$  tight focusing of higher-order Laguerre–Gaussian radially polarized beam," *Opt. Lett.* **38**(19), 3937–3940 (2013).
37. S. Wang, Y. Cao, and X. Li, "Generation of uniformly oriented in-plane magnetization with near-unity purity in 4pi microscopy," *Opt. Lett.* **42**(23), 5050–5053 (2017).
38. W. Yan, Z. Nie, X. Liu, G. Lan, X. Zhang, Y. Wang, and Y. Song, "Dynamic control of transverse magnetization spot arrays," *Opt. Express* **26**(13), 16824–16835 (2018).
39. Z. Man, S. Fu, and G. Wei, "Focus engineering based on analytical formulae for tightly focused polarized beams with arbitrary geometric configurations of linear polarization," *J. Opt. Soc. Am. A* **34**(8), 1384–1391 (2017).
40. B. Richards and E. Wolf, "Electromagnetic diffraction in optical systems II. Structure of the image field in an aplanatic system," *Proc. R. Soc. Lond. A* **253**(1274), 358–379 (1959).
41. M. V. Berry, "Index formulae for singular lines of polarization," *J. Opt. A: Pure Appl. Opt.* **6**(7), 675–678 (2004).

42. T. Bauer, P. Banzer, E. Karimi, S. Orlov, A. Rubano, L. Marrucci, E. Santamato, R. W. Boyd, and G. Leuchs, "Observation of optical polarization Möbius strips," *Science* **347**(6225), 964–966 (2015).
43. T. Bauer, M. Neugebauer, G. Leuchs, and P. Banzer, "Optical Polarization Möbius Strips and Points of Purely Transverse Spin Density," *Phys. Rev. Lett.* **117**(1), 013601 (2016).
44. S. Vyas, Y. Kozawa, and S. Sato, "Polarization singularities in superposition of vector beams," *Opt. Express* **21**(7), 8972–8986 (2013).